

# Discovery of Atomic Clock-Like Spin Defects in Simple Oxides from First Principles

Joel Davidsson,<sup>1,\*</sup> Mykyta Onizhuk,<sup>2,†</sup> Christian Vorwerk,<sup>2</sup> and Giulia Galli<sup>3,4,‡</sup>

<sup>1</sup>*Department of Physics, Chemistry and Biology,  
Linköping University, SE-581 83 Linköping, Sweden*

<sup>2</sup>*Pritzker School of Molecular Engineering, University of Chicago, Chicago, Illinois 60637, United States*

<sup>3</sup>*Pritzker School of Molecular Engineering and Department of Chemistry, University of Chicago, Chicago IL 60637, USA*

<sup>4</sup>*Materials Science Division and Center for Molecular Engineering,  
Argonne National Laboratory, Lemont IL 60439, USA*

Virtually noiseless due to the scarcity of spinful nuclei in the lattice, simple oxides hold promise as hosts of solid-state spin qubits. However, no suitable spin defect has yet been found in these systems. Using high-throughput first-principles calculations, we predict spin defects in calcium oxide with electronic properties remarkably similar to those of the NV center in diamond. These defects are charged complexes where a dopant atom — Sb, Bi, or I — occupies the volume vacated by adjacent cation and anion vacancies. The predicted zero phonon line shows that the Bi complex emits in the telecommunication range, and the computed many-body energy levels suggest a viable optical cycle required for qubit initialization. Notably, the high-spin nucleus of each dopant strongly couples to the electron spin, leading to many controllable quantum levels and the emergence of atomic clock-like transitions that are well protected from environmental noise. Specifically, the Hanh-echo coherence time increases beyond seconds at the clock-like transition in the defect with <sup>209</sup>Bi. Our results pave the way to designing quantum states with long coherence times in simple oxides, making them attractive platforms for quantum technologies.

## I. INTRODUCTION

Point defects in semiconductors and insulators, and their associated electron and nuclear spins, are key components of quantum information systems [1, 2]. In the last two decades, several defects and host crystals have been proposed [1], which are suitable for quantum technologies. Notable examples are the NV center in diamond [3–10] and the divacancy in silicon carbide [11–14], that exhibit excellent coherence properties for quantum sensing and communication. However, the search and engineering of spin defects in solids that can combine *multiple* quantum functionalities, such as computation, communication, and sensing are still open challenges.

Among promising classes of materials for the implementation of different quantum modalities are oxides and chalcogenides. Recent theoretical predictions [15] suggest that spin defects in simple oxides, such as MgO and CaO, should have nuclear spin-limited coherence times at least ten times longer than those measured in naturally abundant diamond and SiC for the NV center and the divacancy, respectively. Importantly, in oxides, quantum coherence properties could be engineered by interfacing them with magnetic, strain, and electric fields, providing a broad parameter space over which optimization of desired functionalities may be carried out. In addition, interfacing oxides with semiconductors offers the possibility of engineering hybrid quantum optoelectronic systems, as well as the flexibility of tuning materials properties, e.g. with specific strain fields.

An essential prerequisite to designing and engineering quantum platforms using oxides is the availability of spin defects with the desired electronic properties, in addition to long coherence times. The discovery and prediction of such defects is clearly a challenging task, given the immensely vast parameter space to explore.

Here, we focus on a specific oxide, calcium oxide (CaO) that has the potential to host spin defects with Hahn-echo coherence time ( $T_2$ ) of 34 ms [15] i.e. 30 to 40 times longer than in natural SiC or diamond, respectively. CaO contains minimal nuclei with non-zero spins in the naturally abundant material, and it was also identified as a promising candidate for spin qubits in a recent search of inorganic materials [16], although suitable spin defects have not yet been predicted.

In this paper, we use a high-throughput method [17, 18] and calculations based on density functional theory, quantum embedding theory [19, 20], and spin dynamics calculations using the cluster-correlation expansion method (CCE) [21]. Using this combination of techniques, we predict point defects in CaO with electronic properties remarkably similar to those of the NV center in diamond. In addition, these defects emit in the telecommunication range and exhibit improved coherence times due to the presence of clock transitions. Our results pave the way to engineering quantum states with long coherence times in simple oxides.

## II. RESULTS

We adopt a high-throughput method that has been successfully applied to the search of spin defects in SiC [22, 23], and we use the software Automatic Defect Analysis and Qualification (ADAQ) [17, 18] to gen-

\* joel.davidsson@liu.se

† onizhuk@uchicago.edu

‡ gagalli@uchicago.edu

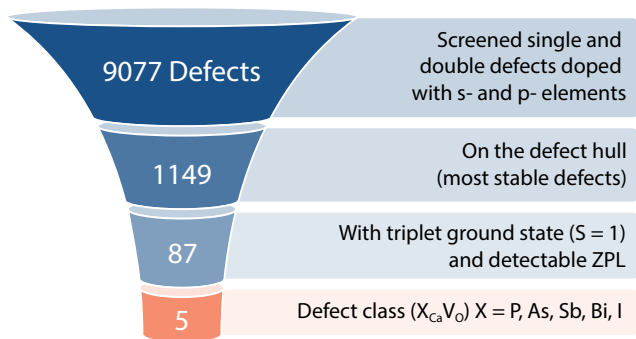


FIG. 1. **High-throughput search.** The selection process of point defects in calcium oxide adopted in the high-throughput search used in this work (see text). We identified five defects denoted as  $X_{Ca}V_O$  (bottom part of the figure) with detectable zero-phonon line (ZPL) and electronic structures similar to that of the NV center in diamond, where the dopant  $X = P, As, Sb, Bi, I$  is located between adjacent Ca and O vacancies.

erate single (vacancies, substitutionals, and interstitials) and double defects (such as vacancy-substitutional clusters) in CaO, a simple oxide with the rocksalt structure. We consider all non-radioactive elements in the  $s$ - and  $p$ -block of the periodic table (details in the Methodology Section). Our strategy is shown in Figure 1. We screen a total of 9077 defects using DFT at the generalized gradient corrected (GGA) level of theory [24], of which 1149 are found on the defect hull (these defects exhibit the lowest formation energy per stoichiometry and for a given Fermi energy [22, 23]). Within the set of most stable defects, we search for those with a triplet ground state ( $S = 1$ ), and we identify 200 candidates; of these, 87 exhibit at least one occupied and one unoccupied localized defect state in the band gap, indicating that a zero phonon line (ZPL) should be detectable experimentally. Finally, a careful investigation of these 87 candidates reveals a class of five stable defects ( $X_{Ca}V_O$ ), which we call NV-like, with an electronic structure similar to that of the NV center in diamond. They consist of a Schottky defect, specifically an oxygen  $V_O$  and adjacent calcium vacancy  $V_{Ca}$ , and of a dopant atom  $X$  belonging either to group 15 or group 17 of the periodic table:  $X = P, As, Sb, Bi, I$ . For  $X$  belonging to group 15, the NV-like defects are negatively charged,  $X_{Ca}V_O^-$  and, as shown in Fig. 2a, the equilibrium position of the dopant is along the shortest path connecting the Ca and O vacancies, closer to the position of the missing Ca atom. For  $X=P$  and  $As$ , we find two local minima along the  $V_{Ca}$  and  $V_O$  path, but only the configuration closest to the Ca site, which has the lowest energy, exhibits the desired electronic structure. However, we could not obtain a satisfactory convergence of the excited states for  $P$  and  $As$  (see Supplementary Note 1 for more details), hence in the following, we only focus on  $Sb$  and  $Bi$ . Interestingly, the  $N_{Ca}V_O^-$  (the direct analog to the NV center), with a triplet ground state, does not have the desired electronic structure since N oc-

cupies the O site ( $V_{Ca}N_O$ ). For dopants of group 17, we find that only the positively charged  $I_{Ca}V_O$  complex is stable and has the same electronic structure as that of the group 15 dopants, with  $I$  located in a similar position as  $Sb$  and  $Bi$ .

The geometrical configuration of the NV-like defects identified here has  $C_{4v}$  symmetry (see Figure 2) and gives rise to four states within the band gap in both spin channels. One is close to the valence band maximum; the other three are mid-gap states. For example, for  $X$  from group 15, the mid-gap states originate from the single substitutional  $X_O^-$  that has  $O_h$  symmetry and a three-fold degenerate state ( $T_{1u}$ ). As mentioned above, the most stable position of the  $X$  dopant in  $X_{Ca}V_O$ , in the absence of the adjacent Ca, is between the Ca and O vacancy sites (Figure 2a). This geometrical configuration lowers the  $O_h$  symmetry of the complex to  $C_{4v}$ , leading to a split of the  $T_{1u}$  into  $a_1$  and  $e$  states; as shown in Figure 2c), these states are highly localized.

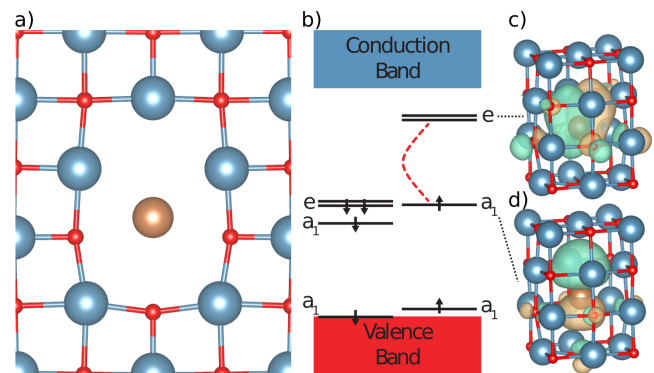


FIG. 2. **Structural and electronic properties of predicted defects.** a) Atomic configuration of the  $X_{Ca}V_O$  defects identified in our search (see Figure 1), where  $X=Sb, Bi, I$  is located between the missing cation and anion sites. For  $X=Sb$  or  $Bi$ , the defect is negatively charged; for  $X=I$ , it is positively charged. All defects have  $C_{4v}$  symmetry. Red, blue and brown spheres denote oxygen, calcium and dopant atoms, respectively. b) Electronic structure of the  $X_{Ca}V_O$  complexes, where we have indicated the zero-phonon line excitation between the  $a_1$  and  $e$  states. States are labeled following the representation of the  $C_{4v}$  group. c) and d) show the iso-surfaces of the sum of  $e_x$  and  $e_y$  defect orbitals, and of the  $a_1$  defect orbital, respectively, both with a value of  $10^{-4} \text{ \AA}^{3/2}$ .

Figure 3 shows the formation energy of the  $X_{Ca}V_O$  complex and of the separate  $X_{Ca} + V_O$  defects with  $X=Sb, Bi, I$ , as obtained with the HSE functional with a mixing parameter ( $\alpha$ ) of 62.5%. The mixing parameter was chosen to reproduce the experimentally measured band gap of CaO (details are reported in the Supplementary Note 2 and 3, together with a comparison of results obtained at the PBE and HSE level of theory). The shaded regions of Figure 3 indicate the values of the Fermi level ( $E_F$ ) for which NV-like defects are stable and correspond to n-type conditions for  $Sb$  and  $Bi$  and p-type conditions for  $I$ . In CaO, n-type conditions

could be obtained, for example, by substituting Mo with Ca [25]. The Fermi level could also be adjusted by using a Schottky diode as, e.g., in deep-level transient spectroscopy [26]. However, the Fermi level should be adjusted in a range where single intrinsic defects are stable. We investigated the range of stability of intrinsic defects to determine which growth conditions (Ca- or O-rich) are most suitable for X=Sb, Bi, I (see Supplementary Note 3). We found Ca-rich conditions are required to stabilize the Sb and Bi defects in the negative charge state, which has spin-1. Instead O-rich conditions are required for the I defect to be stable in the positive charge that has spin-1. Under appropriate growth conditions, we predict similar formation energies for  $X_{\text{Ca}}\text{V}_{\text{O}}$  in CaO as for the NV center in diamond [27]. Our results indicate that if X is implanted in CaO at high T, where Schottky defects are expected to be present, NV-like defects should be formed upon annealing since the  $X_{\text{Ca}}\text{V}_{\text{O}}$  complex is more stable than the separate  $X_{\text{Ca}}$  and  $\text{V}_{\text{O}}$  point defects.

We now turn to discuss the magneto-optical properties of the NV-like defects identified above, starting with the ZPL, where the excitation of interest is between the  $a_1$  and  $e$  states, as shown in Figure 2b). We find that the  $\text{Bi}_{\text{Ca}}\text{V}_{\text{O}}^-$  defect has a ZPL in the telecommunication range, and  $\text{I}_{\text{Ca}}\text{V}_{\text{O}}^+$  has a ZPL close to the same range.

TABLE I. Computed properties of CaO and the  $X_{\text{Ca}}\text{V}_{\text{O}}$  defects, with X=Sb, Bi, I, as obtained with three different density functionals: PBE, HSE and K-PBE0. We show the band gap, the zero-phonon lines (ZPL), the sum of the ionic displacements between the ground and excited state ( $\Delta\text{R}$ ), and the zero-field splitting (ZFS).

Host/ Defect	Property	Functional		
		PBE	HSE	K-PBE0
CaO	Band gap [eV]	3.64	5.32	6.44
$\text{Sb}_{\text{Ca}}\text{V}_{\text{O}}^-$	ZPL [eV]	0.54	0.53	0.53
	$\Delta\text{R}$ [Å]	0.49	0.52	0.53
	ZFS [GHz]	2.51	2.91	2.96
$\text{Bi}_{\text{Ca}}\text{V}_{\text{O}}^-$	ZPL [eV]	0.75	0.76	0.77
	$\Delta\text{R}$ [Å]	0.49	0.50	0.51
	ZFS [GHz]	2.18	2.46	2.49
$\text{I}_{\text{Ca}}\text{V}_{\text{O}}^+$	ZPL [eV]	0.79	0.78	0.69
	$\Delta\text{R}$ [Å]	0.44	0.60	0.64
	ZFS [GHz]	2.96	3.42	3.48

The band gap of CaO (7.09 eV [28]) is severely underestimated when using the PBE functional (see Table I) and moderately so with the hybrid functionals HSE and K-PBE0. However, remarkably, we find approximately the same ZPL results with all functionals, except in the case of the I dopant (where differences are nevertheless within 10%). These results indicate that in an ionic material such as CaO, Coulombic interactions are dominant in determining the ZPL, and the exchange-correlation interactions have a minor effect on total energy differences.

Interestingly, we observe minor variations among the functionals for the computed geometries in the ground and excited states and the zero-field splitting. The sum of

the ionic displacements between the ground and excited state ( $\Delta\text{R}$ ) increases when using the HSE and K-PBE0 functional instead of PBE. Not unexpectedly, the same trend is seen for the zero-field splitting (ZFS). The geometry difference also affects single-particle orbitals that, in turn, affect the value of the computed dipole-dipole term of the ZFS.

To further characterize the excitations of NV-like defects, we determined the singlet-triplet (S-T) splitting for the most promising complex, emitting in the telecommunication range:  $\text{Bi}_{\text{Ca}}\text{V}_{\text{O}}^-$ . Due to the strong correlation between the localized defect orbitals, the S-T splitting cannot be described using mean field theories, such as DFT. Therefore, we employed the quantum defect embedding theory (QDET) [19], which has been shown to yield accurate results for several spin defects in wide band-gap semiconductors [10, 20]. Our results, displayed in Fig. 4, confirm that the ground state of the defect is a triplet ( $S = 1$ ), as obtained with DFT. The lowest triplet excitation ( $^3\text{E}$ ) is found at 1.45 eV above the ground state ( $^3\text{A}_2$ ). This energy is similar to the DFT absorption energy (varying between 1.2 and 1.3 eV, depending on the functional). Within the computed many-body states, we identify three singlet ( $S = 0$ ) excitations. Two nearly degenerate singlet states ( $^1\text{B}_1$  and  $^1\text{B}_2$ ) occur at 0.26 eV and 0.33 eV above the ground state, while a non-degenerate singlet state ( $^1\text{A}_1$ ) is at 0.56 eV. This many-body level diagram resembles that of the NV center in diamond [27], where two singlet excited states occur between the triplet ground state and the first triplet excited state (see Fig. 4). Since both defects have  $^3\text{A}_2$  ground states and similar ZFS value, they both split into  $\text{A}_1$  and  $\text{E}$  states. To estimate the spin-orbit interaction of the  $^3\text{E}$  states, we assume that the interaction parameters of  $\text{Bi}_{\text{Ca}}\text{V}_{\text{O}}^-$  in CaO are similar in sign and magnitude as that of the NV center [27], and with this hypothesis, which remains to be verified, we find the order reported in Fig. 4. For the NV center, an optical cycle populates the  $m_s = 0$  instead of the  $m_s = \pm 1$  states, due to inter-system crossing mediated by phonons and spin-orbit interaction [27]. Our results indicate that there should be such a cycle for the NV-like defects in CaO as well.

As mentioned in the introduction, unlike diamond, CaO is an almost noiseless host of spin-defects, removing the need for any isotopic engineering. Natural-abundant CaO contains only about 0.13% of magnetic nuclei  $^{43}\text{Ca}$  with spin- $7/2$  and about 0.04% of spin- $5/2$   $^{17}\text{O}$ . As a result, the nuclear-spin limited Hahn-echo  $T_2$  of the localized electron spin in CaO is 34 ms, an order of magnitude higher than of naturally abundant diamond (0.89 ms) [15]. A significant additional advantage of the defect centers discovered here is that each of them contains a *single* nuclear spin that strongly couples to the electron spin of the defect. For example,  $^{209}\text{Bi}$  is a spin- $9/2$  particle with nearly 100% natural abundance. The parallel component of the hyperfine coupling between the electron and Bi nuclear spins, 1.27 GHz, is similar to Bi donors in Si [29]. Hence, the combined electron-nuclear system ex-

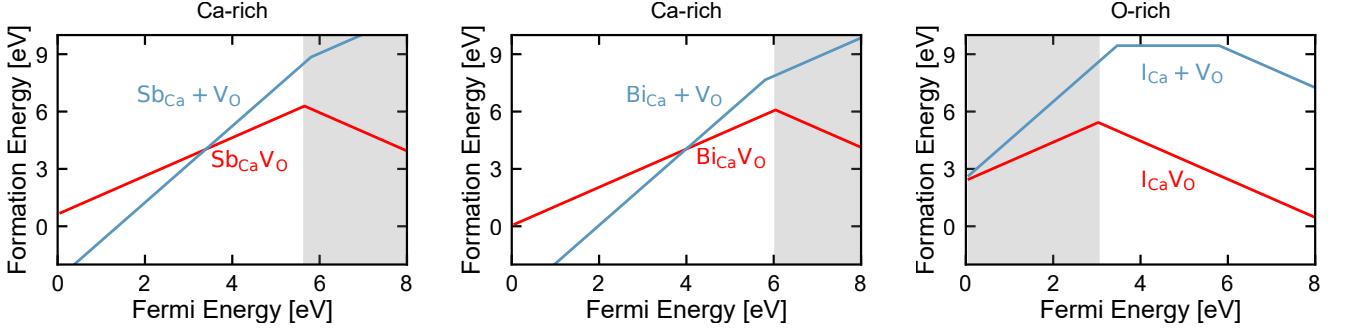


FIG. 3. **Formation energies of predicted defects.** Each panel shows the formation energy for the  $X_{\text{Ca}}\text{V}_\text{O}$  defects where  $X = \text{Sb}, \text{Bi}, \text{I}$ , obtained at the HSE level of theory with 62.5% short-range Hartree-Fock exchange (for PBE and HSE results, see Supplementary Figure 2). Red lines are the formation energy for the complexes.  $\text{Sb}_{\text{Ca}}\text{V}_\text{O}^-$ ,  $\text{Bi}_{\text{Ca}}\text{V}_\text{O}^-$ , and  $\text{I}_{\text{Ca}}\text{V}_\text{O}^+$  are stable for values of the Fermi level indicated by the shaded regions and have the electronic structure shown in Figure 2b). The blue lines are the formation energy for the separated single defects ( $X_{\text{Ca}} + \text{V}_\text{O}$ ). When the red line is below the blue, the complex has a positive binding energy. The Sb and Bi defects require Ca-rich conditions to be stable in the negatively charged state, whereas the I defect requires O-rich conditions (see Supplementary Note 3 for details).

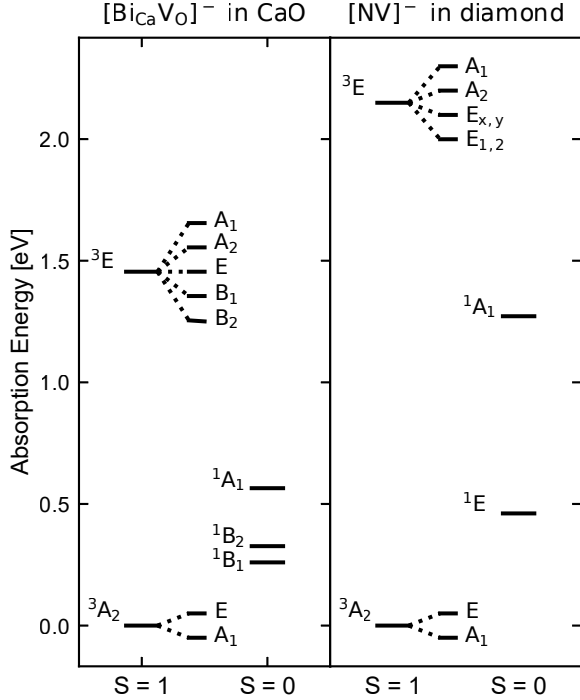


FIG. 4. **Many-body states from quantum embedding.** Many-body state diagram for the  $\text{Bi}_{\text{Ca}}\text{V}_\text{O}^-$  defect in CaO (left) compared to that of the  $\text{NV}^-$  defect in diamond (right). Excitation energies are obtained using the quantum defect embedding theory (QDET). The splitting of the  $^3\text{A}_2$  and  $^3\text{E}$  states is due to ZFS and spin-orbit coupling, respectively. The diamond results are taken from Ref. 19 and the symmetries from Ref. 27.

hibits 30 energy levels (see Fig 5a) that are separately addressable in experiments, providing a broad space of spin states accessible for the design of quantum technologies.

The strong electron-nuclear spin coupling in  $\text{Bi}_{\text{Ca}}\text{V}_\text{O}^-$  leads to a set of avoided crossings between energy levels as a function of the magnetic field. The spin transitions between these levels, known as "clock transitions" (CT) [29], are remarkably robust to external perturbations, and thus the coherence time of qubits operating at a CT can be substantially increased [30, 31]. Using the cluster-correlation expansion method (CCE), implemented in the PyCCE code [21], we computed the coherence of the spin qubit  $\text{Bi}_{\text{Ca}}\text{V}_\text{O}^-$  near CTs (see Fig. 5b). We find that at the magnetic field of 22.18 mT ( $2 \mu\text{T}$  from a clock transition), the  $T_2$  is already increased by two orders of magnitude (4.7 seconds) compared to that of a qubit operating away from CTs (34 ms).

### III. DISCUSSION

Table II summarizes the predicted physical properties of the NV center in diamond and those of the NV-like defects in CaO, for which we choose a specific functional, HSE, that has yielded results in good agreement with experiments for diamond. In CaO, the electron spin is predicted to have longer Hahn-echo  $T_2$  (34 ms) than in naturally abundant diamond (0.89 ms) [15]. Furthermore, the refractive index of CaO (1.84) is lower than that of diamond (2.42) and closer to the refractive index of optical fibers (1.44), thus enabling an increase in the number of emitted photons into the fiber, if the two materials are integrated.

The computed ZPL for the NV center is 2.00 eV, which is in close agreement with the experimental value of 1.945 eV [33], and, as discussed above, those of the NV-like defects in CaO are in the range 0.53-0.78 eV. The ZPL polarization is perpendicular to the axis of the defect (if the defect is aligned with the z-axis, the transition dipole moment is in the xy-plane). Due to the symmetry of the

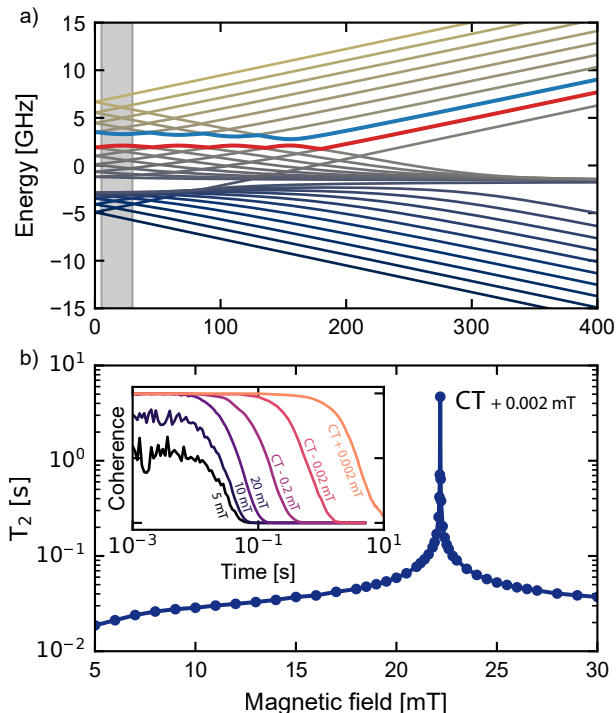


FIG. 5. **Spin dynamics calculations.** a) Spin energy levels of the  $\text{Bi}_{\text{Ca}}\text{V}_{\text{O}}^-$  defect. Levels chosen as qubit levels are marked with red and blue. Grey shaded area represents the range of magnetic fields shown in (b). b) Nuclear spin-limited  $T_2$  of the electron spin near a clock transition (CT), as computed using the CCE method. The inset shows actual computed coherence signal near a clock transition.

TABLE II. Comparison between computed properties of the NV center in diamond and the  $\text{X}_{\text{Ca}}\text{V}_{\text{O}}$  defects in CaO, with  $\text{X}=\text{Sb}$ ,  $\text{Bi}$ , and  $\text{I}$ , as obtained using the HSE functional. We show the zero-phonon line (ZPL), zero field splitting (ZFS), transition dipole moment (TDM), the sum of the ionic displacements between the ground and excited state ( $\Delta\text{R}$ ), and the weighed sum by each ion mass ( $\Delta\text{Q}$ ), and radiative lifetimes.

Host	Diamond	CaO		
$T_2$ time [15] [ms]	0.89	34		
Refractive index	2.42	1.84 [32]		
Defect	$\text{NV}^-$	$\text{Sb}_{\text{Ca}}\text{V}_{\text{O}}^-$	$\text{Bi}_{\text{Ca}}\text{V}_{\text{O}}^-$	$\text{I}_{\text{Ca}}\text{V}_{\text{O}}^+$
Symmetry	$\text{C}_{3v}$	$\text{C}_{4v}$	$\text{C}_{4v}$	$\text{C}_{4v}$
ZPL [eV]	2.00	0.53	0.76	0.78
ZPL [nm]	619	2338	1624	1593
TDM [Debye <sup>2</sup> ]	48	1205	118	1748
Radiative lifetime [ns]	6.5	18	63	4.0
$\Delta\text{R}$ [Å]	0.20	0.52	0.50	0.60
$\Delta\text{Q}$ [ $\text{amu}^{1/2}\text{Å}$ ]	0.70	5.10	6.22	5.49
ZFS [GHz]	3.42	2.91	2.46	3.42

host, the  $\text{X}_{\text{Ca}}\text{V}_{\text{O}}$  defects can be oriented in three different directions, indicating that in experiments a similar polarization will be measured in all directions. The radiative

lifetimes are comparable between NV centers and NV-like defects, all in the ns range. Note, that non-radiative effects were not considered in our study. The computed NV center radiative lifetime (6.5 ns) is close to the experimental value (10 ns [34]), which can be considered as the average between the spin-selected lifetimes of 7.8 ( $m_s = 0$ ) and 12.0 ( $m_s = \pm 1$ ) ns [35]. Our results indicate that of all NV-like defects, the  $\text{Bi}_{\text{Ca}}\text{V}_{\text{O}}^-$  complex is expected to have a bright emission in the telecommunication range (L-band 1565-1625 nm [36]).

The  $\Delta\text{R}$  and  $\Delta\text{Q}$  (the sum of the ionic displacements between the ground and excited states weighed by each ion mass) for the NV center agree with previously calculated values [37]. For the  $\text{X}_{\text{Ca}}\text{V}_{\text{O}}$  defects,  $\Delta\text{R}$ s are larger and  $\Delta\text{Q}$ s are much larger than the corresponding values in diamond, due to the size of the dopants. We find that the dopant displacement between the ground and excited state accounts for most of the  $\Delta\text{R}$  values (75-85%). The large  $\Delta\text{Q}$ s indicate undesirable, large Huang-Rhys (HR) factors ( $S_k \propto \omega_k q_k^2$  [37]), which point at small Debye-Waller factors, indicating a low quantum efficiency, i.e., the ZPL intensity is expected to be weak compared to that of the phonon sideband. Based on our results, the Debye-Waller factors for the  $\text{X}_{\text{Ca}}\text{V}_{\text{O}}$  defects are expected to be much smaller than that of the NV center in diamond ( $\sim 3\%$ ), which is not ideal for quantum technology applications. However, Debye-Waller factors may be enhanced with nanostructuring, as demonstrated for the silicon vacancy in SiC [38] where the factor was increased from 6% in bulk to 58% in nanowires. Our phonon calculations (see Supplementary Note 4 and 5) indicate that the most delocalized bulk phonons (those with an inverse participation ratio below 0.01) are responsible for the large HR factor, indicating that thin films and nanostructured CaO may have more favorable HR and DW factors and ZPL better separated from phonon sidebands (see Supplementary Figure 5).

We find that the theoretical ZFS results for the  $\text{X}_{\text{Ca}}\text{V}_{\text{O}}$  defects and the NV center are comparable. The calculated ground state ZFS (3.42) for the NV center in diamond is higher than the previously calculated value (2.88) [39] (due to approximations discussed in the Methodology section). We assume that this overestimation also applies to the  $\text{X}_{\text{Ca}}\text{V}_{\text{O}}$  defects in CaO, hence we expect that the experimental ZFS of NV-like defects is likely 20% smaller compared to the value obtained in our calculations.

Experimental validation of our results should be relatively straightforward, given the ease of growth of CaO. The material has been epitaxially grown by Molecular Beam Epitaxial (MBE) or related techniques for at least two decades [40, 41], although care must be exercised as samples need to be protected from moisture exposure since  $\text{Ca}(\text{OH})_2$  may readily form. In addition, techniques to implant Bi in CaO are available [42, 43].

In summary, several simple oxides, particularly CaO, have been predicted to be promising hosts of spin defects with long coherence times. Using a high-throughput

search based on first principles calculations, we predicted a class of spin defects in CaO with properties remarkably similar to those of the NV center in diamond. Such NV-like defects ( $X_{\text{Ca}}V_{\text{O}}$ ) consist of a missing Ca-O pair and a dopant  $X=\text{Sb, Bi, and I}$ ; they are stable, with a triplet ground state, in their negatively charged (Sb, Bi) and positively charged (I) states. They also exhibit two singlet excited states between the ground and first triplet excited states, as explicitly verified in the case of Bi, suggesting the possibility of an optical cycle similar to that of the NV center. Importantly, the  $X_{\text{Ca}}V_{\text{O}}$  complexes have a detectable zero phonon line close to the telecommunication range and exhibit a zero-field splitting similar to the NV center in diamond. In particular, we predict that the  $\text{Bi}_{\text{Ca}}V_{\text{O}}^-$  complex has a bright emission in the L-band. In addition, the presence of a high spin nucleus, strongly coupled to the electron spin, leads to many spin levels addressable in experiments and to the emergence of avoided crossings in the spin energy spectrum. We showed that when operating at these avoided crossings, the spin coherence of the  $\text{Bi}_{\text{Ca}}V_{\text{O}}^-$  complex is increased by at least two orders of magnitude, exceeding seconds. In closing, the results presented in our paper pave the way to designing and engineering quantum states with long coherence times in CaO and other simple oxides.

## METHODS

The defects in CaO were created using the ADAQ [17, 18] software package and the high-throughput toolkit [44]. These include vacancies, substitutionals, and interstitials, as well as pair combinations of all single defects. The maximum distance between double defects was set to 8.5 Å, which corresponds approximately to the fourth nearest neighbor distance in CaO. The dopants were limited to all non-radioactive elements in the  $s$ - and  $p$ -block of the periodic table. Using these settings, we generated 15446 defects. We then omitted interstitial-interstitial clusters (6581), and were left with 9077 defects that were processed in the automatic screening workflow present in ADAQ, see Ref. 17 for more details.

The lattice parameter of CaO was optimized with the PBE functional and found to be 4.829 Å, which is close to the experimental value of 4.811 Å [45]. We used supercells with 512 atoms for CaO and diamond. In the case of CaO, considering a dielectric constant of 11.95, we obtained a Lany-Zunger charge correction [46] of  $0.058 \cdot q^2$  eV (see Supplementary Note 3A for more details). We assumed that the choice of the functional (semi-local or hybrid) and charge corrections do not affect the formation energy trend of defects obtained at the PBE level of theory.

The computations were performed with the Vienna Ab initio Simulation Package (VASP) [47, 48] with the gamma compiled version 5.4.4, which uses the projector augmented wave (PAW) [49, 50] method. We used three

different functionals: the semi-local exchange-correlation functional of Perdew, Burke, and Ernzerhof (PBE) [24], the screened hybrid functional of Heyd, Scuseria, and Ernzerhof (HSE06) [51, 52] with the standard mixing parameter  $\alpha$  set to the standard value (25%) and (62.5%, more details in Supplementary Note 3), and the K-PBE0 [53] functional (no range separation) with  $\alpha = 0.29$ . In ADAQ, the plane wave energy and kinetic energy cutoff of PBE calculations were set to 600 and 900 eV, respectively. For the hybrid calculations, these were reduced to 400 and 800 eV, respectively. The total energy criterion was set to  $10^{-6}$  eV for PBE, and  $10^{-4}$  eV in ADAQ and for the hybrid calculations. The structural minimization criterion is set to  $5 \times 10^{-5}$  eV for PBE,  $5 \times 10^{-3}$  eV for ADAQ, and  $10^{-2}$  eV/Å for the hybrid calculations. Gaussian smearing and  $\Psi_k = \Psi_{-k}^*$  are used. The pseudopotentials from VASP folder dated 2015-09-21 are Ca\_pv, O, N, As\_d, P,Sb, Bi\_d, I, and C.

The ZPLs and absorption energies are calculated using constrained DFT ( $\Delta$ -SCF) [54] for each functional. The TDMs between the ground and excited state are calculated using the wave functions from the relaxed ground and excited state, which provide an accurate polarization and lifetime [55]. The ion relaxation between the ground and excited state are characterized by  $\Delta R = \sum_i (R_{\text{ex},i} - R_{\text{gr},i})$  and  $\Delta Q^2 = \sum_i m_i (R_{\text{ex},i} - R_{\text{gr},i})^2$ , where  $R_i$  is the ionic position and  $m_i$  is the ionic mass [37]. The ZFSs are calculated using the dipole-dipole interaction of the spins [39], as implemented in VASP. We note that the method in Ref. 39 uses a stand-alone code that calculates the ZFS only from the pseudo partial waves, whereas the implementation in VASP includes all contributions. The overestimate between the theory and experiment obtained using the VASP implementation for the NV center is expected to be similar for the NV-like defects in CaO.

Quantum Defect Embedding Theory (QDET) calculations are performed using the WEST (Without Empty States) code [56]. In QDET, an active space is formed by localized defect orbitals. The normalization of the single-particle levels in the active space and the screening of the Coulomb interaction within the active space due to the remaining environment is determined from many-body perturbation theory calculations. In QDET, an effective Hamiltonian in second quantization is formulated, the diagonalization of which yields the excitations of orbitals belonging to the active space. For more methodological details, see Refs. [19]

As a starting point for the QDET calculations, DFT electronic-structure calculations are performed using the Quantum Espresso code. Due to the high computational cost of QDET, calculations are performed for defected supercells with 53, 63, and 215 atoms. We have carefully analyzed the convergence both of the defect geometry and the QDET excitations with supercell size.

Nuclear spin bath-limited spin coherence was computed using the coupled cluster expansion (CCE) approach with the PyCCE package [21]. The CCE method



approximates the coherence as a product of irreducible cluster contributions:

$$\mathcal{L}(t) = \prod_C \tilde{L}_C(t) = \prod_i \tilde{L}_{\{i\}}(t) \prod_{i,j} \tilde{L}_{\{ij\}}(t) \dots \quad (1)$$

where  $\tilde{L}_{\{i\}}(t)$  is the contribution of a single bath spin  $i$ ,  $\tilde{L}_{\{ij\}}(t)$  is a contribution of a spin pair  $i, j$  and so on. More details are available in Ref. 57 and 58. The CCE approach was successfully applied to the Bi-based systems before, specifically Bi donor in Si, see Ref. 31, 59, and 60. In the current work, we find that the coherence function converges at the third order of CCE with Monte Carlo bath state sampling [30] up to 2 mT away from the clock transition. The coherence functions, computed using CCE and generalized CCE (gCCE[30]), are identical in this system.

#### DATA AVAILABILITY

The ADAQ high-throughput data are available at <https://httk.org/adaq/>.

#### ACKNOWLEDGEMENT

We thank Vrindaa Somjit for many useful discussions. J.D. acknowledges support from the Swedish e-science Research Centre (SeRC), the Knut and Alice Wallenberg Foundation through the WBSQD2 project (Grant No. 2018.0071), and the Swedish Research Council (VR) Grant No. 2022-00276. M.O. acknowledges the support

from a Google PhD Fellowship and a fellowship by the Qubbe center, which is supported by the National Science Foundation. C.V. and G.G. acknowledge support from the Air Force Office of Scientific Research (AFOSR) through the CFIRE grant # FA95502310667. This work used the WEST and pyCCE codes whose development is supported by MICCoM, which is part of the Computational Materials Sciences Program funded by the U.S. Department of Energy, Office of Science, Basic Energy Sciences, Materials Sciences, and Engineering Division through Argonne National Laboratory.

The DFT computations were enabled by resources provided by the National Academic Infrastructure for Supercomputing in Sweden (NAISS), partially funded by the Swedish Research Council through grant agreement no. 2022-06725. The QDET calculations using the WEST code and pyCCE calculations were carried out at the RCC center at the University of Chicago.

#### AUTHOR CONTRIBUTIONS

J.D. conceived the project, with support from the other authors, and performed the high-throughput and hybrid DFT calculations. C.V. performed the quantum embedding calculations. M.O. performed the coherence calculations. G.G. supervised the work. All authors discussed the results, and wrote the manuscript.

#### COMPETING INTERESTS

The authors declare no competing interests.

- 
- [1] G. Zhang, Y. Cheng, J.-P. Chou, and A. Gali, Material platforms for defect qubits and single-photon emitters, *Applied Physics Reviews* **7**, 031308 (2020), <https://doi.org/10.1063/5.0006075>.
- [2] G. Wolfowicz, F. J. Heremans, C. P. Anderson, S. Kanai, H. Seo, A. Gali, G. Galli, and D. D. Awschalom, Quantum guidelines for solid-state spin defects, *Nature Reviews Materials* **6**, 906 (2021).
- [3] G. Davies, M. F. Hamer, and W. C. Price, Optical studies of the 1.945 eV vibronic band in diamond, *Proceedings of the Royal Society of London. A. Mathematical and Physical Sciences* **348**, 285 (1976).
- [4] G. Balasubramanian, P. Neumann, D. Twitchen, M. Markham, R. Kolesov, N. Mizuochi, J. Isoya, J. Achard, J. Beck, J. Tissler, V. Jacques, P. R. Hemmer, F. Jelezko, and J. Wrachtrup, Ultralong spin coherence time in isotopically engineered diamond, *Nature Materials* **8**, 383 (2009).
- [5] S. Choi, M. Jain, and S. G. Louie, Mechanism for optical initialization of spin in NV<sup>-</sup> center in diamond, *Physical Review B* **86**, 041202 (2012).
- [6] M. W. Doherty, N. B. Manson, P. Delaney, and L. C. L. Hollenberg, The negatively charged nitrogen-vacancy centre in diamond: The electronic solution, *New Journal of Physics* **13**, 025019 (2011).
- [7] M. L. Goldman, M. W. Doherty, A. Sipahigil, N. Y. Yao, S. D. Bennett, N. B. Manson, A. Kubanek, and M. D. Lukin, State-selective intersystem crossing in nitrogen-vacancy centers, *Physical Review B* **91**, 165201 (2015).
- [8] J. R. Maze, A. Gali, E. Togan, Y. Chu, A. Trifonov, E. Kaxiras, and M. D. Lukin, Properties of nitrogen-vacancy centers in diamond: The group theoretic approach, *New Journal of Physics* **13**, 025025 (2011).
- [9] L. J. Rogers, S. Armstrong, M. J. Sellars, and N. B. Manson, Infrared emission of the NV centre in diamond: Zeeman and uniaxial stress studies, *New Journal of Physics* **10**, 103024 (2008).
- [10] H. Ma, N. Sheng, M. Govoni, and G. Galli, First-principles studies of strongly correlated states in defect spin qubits in diamond, *Physical Chemistry Chemical Physics* **22**, 25522 (2020).
- [11] J. Davidsson, V. Ivády, R. Armiento, N. T. Son, A. Gali, and I. A. Abrikosov, First principles predictions of magneto-optical data for semiconductor point defect identification: the case of divacancy defects in 4h-sic, *New Journal of Physics* **20**, 023035 (2018).

- [12] J. Davidsson, V. Ivády, R. Armiento, T. Ohshima, N. T. Son, A. Gali, and I. A. Abrikosov, Identification of divacancy and silicon vacancy qubits in 6h-sic, *Applied Physics Letters* **114**, 112107 (2019), <https://doi.org/10.1063/1.5083031>.
- [13] H. Seo, A. L. Falk, P. V. Klimov, K. C. Miao, G. Galli, and D. D. Awschalom, Quantum decoherence dynamics of divacancy spins in silicon carbide, *Nature Communications* **7**, 12935 (2016).
- [14] D. J. Christle, A. L. Falk, P. Andrich, P. V. Klimov, J. U. Hassan, N. Son, E. Janzén, T. Ohshima, and D. D. Awschalom, Isolated electron spins in silicon carbide with millisecond coherence times, *Nature Materials* **14**, 160 (2015).
- [15] S. Kanai, F. J. Heremans, H. Seo, G. Wolfowicz, C. P. Anderson, S. E. Sullivan, M. Onizhuk, G. Galli, D. D. Awschalom, and H. Ohno, Generalized scaling of spin qubit coherence in over 12,000 host materials, *Proceedings of the National Academy of Sciences* **119**, e2121808119 (2022), <https://www.pnas.org/doi/pdf/10.1073/pnas.2121808119>.
- [16] A. M. Ferrenti, N. P. de Leon, J. D. Thompson, and R. J. Cava, Identifying candidate hosts for quantum defects via data mining, *npj Computational Materials* **6**, 126 (2020).
- [17] J. Davidsson, V. Ivády, R. Armiento, and I. A. Abrikosov, Adaq: Automatic workflows for magneto-optical properties of point defects in semiconductors, *Computer Physics Communications* **269**, 108091 (2021).
- [18] Adaq, <https://httk.org/adaq/> (2022), accessed: 2022-04-04.
- [19] N. Sheng, C. Vorwerk, M. Govoni, and G. Galli, Green's Function Formulation of Quantum Defect Embedding Theory, *Journal of Chemical Theory and Computation* **18**, 3512 (2022).
- [20] H. Ma, N. Sheng, M. Govoni, and G. Galli, Quantum Embedding Theory for Strongly Correlated States in Materials, *Journal of Chemical Theory and Computation* **17**, 2116 (2021).
- [21] M. Onizhuk and G. Galli, Pycce: A python package for cluster correlation expansion simulations of spin qubit dynamics, *Advanced Theory and Simulations* **4**, 2100254 (2021), <https://onlinelibrary.wiley.com/doi/pdf/10.1002/adts.202100254>.
- [22] J. Davidsson, *Color Centers in Semiconductors for Quantum Applications: A High-Throughput Search of Point Defects in SiC*, Ph.D. thesis, Linköping University Electronic Press (2021).
- [23] J. Davidsson, R. Babar, D. Shafizadeh, I. G. Ivanov, V. Ivády, R. Armiento, and I. A. Abrikosov, Exhaustive characterization of modified si vacancies in 4h-sic, *Nanophotonics* **11**, 4565 (2022).
- [24] J. P. Perdew, K. Burke, and M. Ernzerhof, Generalized gradient approximation made simple, *Phys. Rev. Lett.* **77**, 3865 (1996).
- [25] F. Stavale, X. Shao, N. Nilus, H.-J. Freund, S. Prada, L. Giordano, and G. Pacchioni, Donor characteristics of transition-metal-doped oxides: Cr-doped mgo versus mo-doped cao, *Journal of the American Chemical Society* **134**, 11380 (2012), pMID: 22741775, <https://doi.org/10.1021/ja304497n>.
- [26] D. V. Lang, Deep-level transient spectroscopy: A new method to characterize traps in semiconductors, *Journal of Applied Physics* **45**, 3023 (2003), [https://pubs.aip.org/aip/jap/article-pdf/45/7/3023/7954457/3023.1\\_online.pdf](https://pubs.aip.org/aip/jap/article-pdf/45/7/3023/7954457/3023.1_online.pdf).
- [27] Ádám Gali, Ab initio theory of the nitrogen-vacancy center in diamond, *Nanophotonics* **8**, 1907 (2019).
- [28] R. Whited, C. J. Flaten, and W. Walker, Exciton thermoreflectance of mgo and cao, *Solid State Communications* **13**, 1903 (1973).
- [29] G. Wolfowicz, A. M. Tyryshkin, R. E. George, H. Riemann, N. V. Abrosimov, P. Becker, H.-J. Pohl, M. L. W. Thewalt, S. A. Lyon, and J. J. L. Morton, Atomic clock transitions in silicon-based spin qubits, *Nature Nanotechnology* **8**, 561 (2013).
- [30] M. Onizhuk, K. C. Miao, J. P. Blanton, H. Ma, C. P. Anderson, A. Bourassa, D. D. Awschalom, and G. Galli, Probing the coherence of solid-state qubits at avoided crossings, *PRX Quantum* **2**, 010311 (2021).
- [31] S. J. Balian, G. Wolfowicz, J. J. L. Morton, and T. S. Monteiro, Quantum-bath-driven decoherence of mixed spin systems, *Phys. Rev. B* **89**, 045403 (2014).
- [32] W. M. Haynes, D. R. Lide, and T. J. Bruno, *CRC handbook of chemistry and physics*, 95th ed. (CRC press, 2016).
- [33] G. Davies and M. Hamer, Optical studies of the 1.945 ev vibronic band in diamond, *Proceedings of the Royal Society of London. A. Mathematical and Physical Sciences* **348**, 285 (1976).
- [34] R. Ulbricht and Z.-H. Loh, Excited-state lifetime of the Nv<sup>-</sup> infrared transition in diamond, *Phys. Rev. B* **98**, 094309 (2018).
- [35] A. Batalov, C. Zierl, T. Gaebel, P. Neumann, I.-Y. Chan, G. Balasubramanian, P. R. Hemmer, F. Jelezko, and J. Wrachtrup, Temporal coherence of photons emitted by single nitrogen-vacancy defect centers in diamond using optical rabi-oscillations, *Phys. Rev. Lett.* **100**, 077401 (2008).
- [36] L. Gasca, From o to l: The future of optical-wavelength bands, *Broadband properties* **6**, 83 (2008).
- [37] A. Alkauskas, B. B. Buckley, D. D. Awschalom, and C. G. V. de Walle, First-principles theory of the luminescence lineshape for the triplet transition in diamond nv centres, *New Journal of Physics* **16**, 073026 (2014).
- [38] J. H. Lee, W. B. Jeon, J. S. Moon, J. Lee, S.-W. Han, Z. Bodrog, A. Gali, S.-Y. Lee, and J.-H. Kim, Strong zero-phonon transition from point defect-stacking fault complexes in silicon carbide nanowires, *Nano Letters* **21**, 9187 (2021).
- [39] V. Ivády, T. Simon, J. R. Maze, I. A. Abrikosov, and A. Gali, Pressure and temperature dependence of the zero-field splitting in the ground state of nv centers in diamond: A first-principles study, *Phys. Rev. B* **90**, 235205 (2014).
- [40] M. D. Losego, S. Mita, R. Collazo, Z. Sitar, and J.-P. Maria, Epitaxial calcium oxide films deposited on gallium nitride surfaces, *Journal of Vacuum Science & Technology B: Microelectronics and Nanometer Structures Processing, Measurement, and Phenomena* **25**, 1029 (2007), [https://pubs.aip.org/avs/jvb/article-pdf/25/3/1029/8215747/1029.1\\_online.pdf](https://pubs.aip.org/avs/jvb/article-pdf/25/3/1029/8215747/1029.1_online.pdf).
- [41] S. Migita, Y. Kasai, and S. Sakai, Molecular beam epitaxial growth of sro and cao with rheed intensity oscillation, *Journal of Low Temperature Physics* **105**, 1337 (1996).
- [42] A. E. Hughes and G. P. Pells, Absorption and luminescence of bismuth ions implanted into cao and mgo single crystals, *physica status solidi (a)* **25**, 437 (1974),



- <https://onlinelibrary.wiley.com/doi/pdf/10.1002/pssa.221025>
- [43] H. Swart and R. Kroon, (invited) ultraviolet and visible luminescence from bismuth doped materials, *Optical Materials: X* **2**, 100025 (2019).
- [44] R. Armiento, Database-Driven High-Throughput Calculations and Machine Learning Models for Materials Design, in *Machine Learning Meets Quantum Physics*, Lecture Notes in Physics, Vol. 968, edited by K. T. Schütt, S. Chmiela, O. A. von Lilienfeld, A. Tkatchenko, K. Tsuda, and K.-R. Müller (Springer International Publishing, Cham, 2020).
- [45] P. Sharma, S. Verma, A. Jain, and N. Kaurav, Theoretical analysis of the structural phase transition in alkaline earth oxides, *AIP Conference Proceedings* **2100**, 020119 (2019), <https://aip.scitation.org/doi/pdf/10.1063/1.5098673>.
- [46] S. Lany and A. Zunger, Assessment of correction methods for the band-gap problem and for finite-size effects in supercell defect calculations: Case studies for zno and gaas, *Phys. Rev. B* **78**, 235104 (2008).
- [47] G. Kresse and J. Hafner, *Ab initio* molecular-dynamics simulation of the liquid-metal–amorphous-semiconductor transition in germanium, *Phys. Rev. B* **49**, 14251 (1994).
- [48] G. Kresse and J. Furthmüller, Efficient iterative schemes for *ab initio* total-energy calculations using a plane-wave basis set, *Phys. Rev. B* **54**, 11169 (1996).
- [49] P. E. Blöchl, Projector augmented-wave method, *Phys. Rev. B* **50**, 17953 (1994).
- [50] G. Kresse and D. Joubert, From ultrasoft pseudopotentials to the projector augmented-wave method, *Phys. Rev. B* **59**, 1758 (1999).
- [51] J. Heyd, G. E. Scuseria, and M. Ernzerhof, Hybrid functionals based on a screened coulomb potential, *J. Chem. Phys.* **118**, 8207 (2003).
- [52] J. Heyd, G. E. Scuseria, and M. Ernzerhof, Erratum: “hybrid functionals based on a screened coulomb potential” [ *J. Chem. Phys.* **118**, 8207 (2003) ], *J. Chem. Phys.* **124**, 219906 (2006).
- [53] J. Yang, S. Falletta, and A. Pasquarello, One-shot approach for enforcing piecewise linearity on hybrid functionals: Application to band gap predictions, *The Journal of Physical Chemistry Letters* **13**, 3066 (2022).
- [54] B. Kaduk, T. Kowalczyk, and T. Van Voorhis, Constrained density functional theory, *Chem. Rev.* **112**, 321 (2012), PMID: 22077560.
- [55] J. Davidsson, Theoretical polarization of zero phonon lines in point defects, *Journal of Physics: Condensed Matter* **32**, 385502 (2020).
- [56] M. Govoni and G. Galli, Large Scale GW Calculations, *Journal of Chemical Theory and Computation* **11**, 2680 (2015).
- [57] W. Yang and R.-B. Liu, Quantum many-body theory of qubit decoherence in a finite-size spin bath, *Phys. Rev. B* **78**, 085315 (2008).
- [58] W. Yang and R.-B. Liu, Quantum many-body theory of qubit decoherence in a finite-size spin bath. ii. ensemble dynamics, *Phys. Rev. B* **79**, 115320 (2009).
- [59] S. J. Balian, R.-B. Liu, and T. S. Monteiro, Keeping a spin qubit alive in natural silicon: Comparing optimal working points and dynamical decoupling, *Phys. Rev. B* **91**, 245416 (2015).
- [60] W.-L. Ma, G. Wolfowicz, S.-S. Li, J. J. L. Morton, and R.-B. Liu, Classical nature of nuclear spin noise near clock transitions of bi donors in silicon, *Phys. Rev. B* **92**, 161403 (2015).

**SUPPLEMENTARY INFORMATION:**

**Discovery of Atomic Clock-Like Spin Defects in Simple Oxides  
from First Principles**

Joel Davidsson,<sup>1,\*</sup> Mykyta Onizhuk,<sup>2,†</sup> Christian Vorwerk,<sup>2</sup> and Giulia Galli<sup>3,4,‡</sup>

<sup>1</sup>*Department of Physics, Chemistry and Biology,  
Linköping University, SE-581 83 Linköping, Sweden*

<sup>2</sup>*Pritzker School of Molecular Engineering,  
University of Chicago, Chicago, Illinois 60637, United States*

<sup>3</sup>*Pritzker School of Molecular Engineering and Department of Chemistry,  
University of Chicago, Chicago IL 60637, USA*

<sup>4</sup>*Materials Science Division and Center for Molecular Engineering,  
Argonne National Laboratory, Lemont IL 60439, USA*

arXiv:2302.07523v4 [cond-mat.mtrl-sci] 11 Jun 2024

---

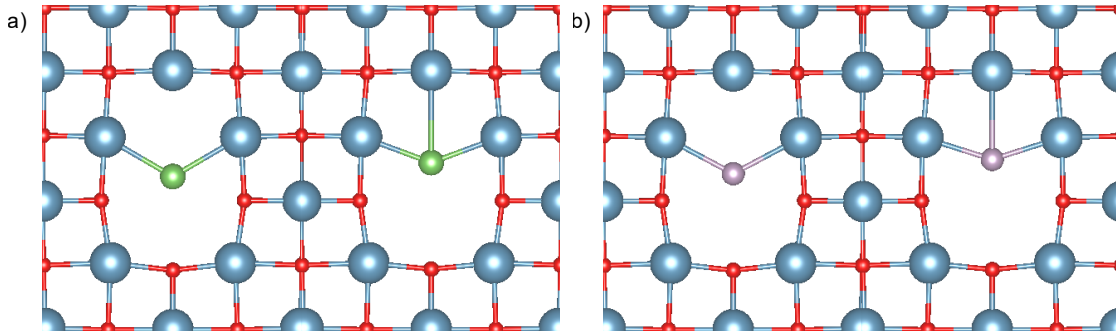
\* joel.davidsson@liu.se

† onizhuk@uchicago.edu

‡ gagalli@uchicago.edu

## SUPPLEMENTARY NOTE 1. POTENTIAL ENERGY SURFACE FOR P AND AS DOPANTS

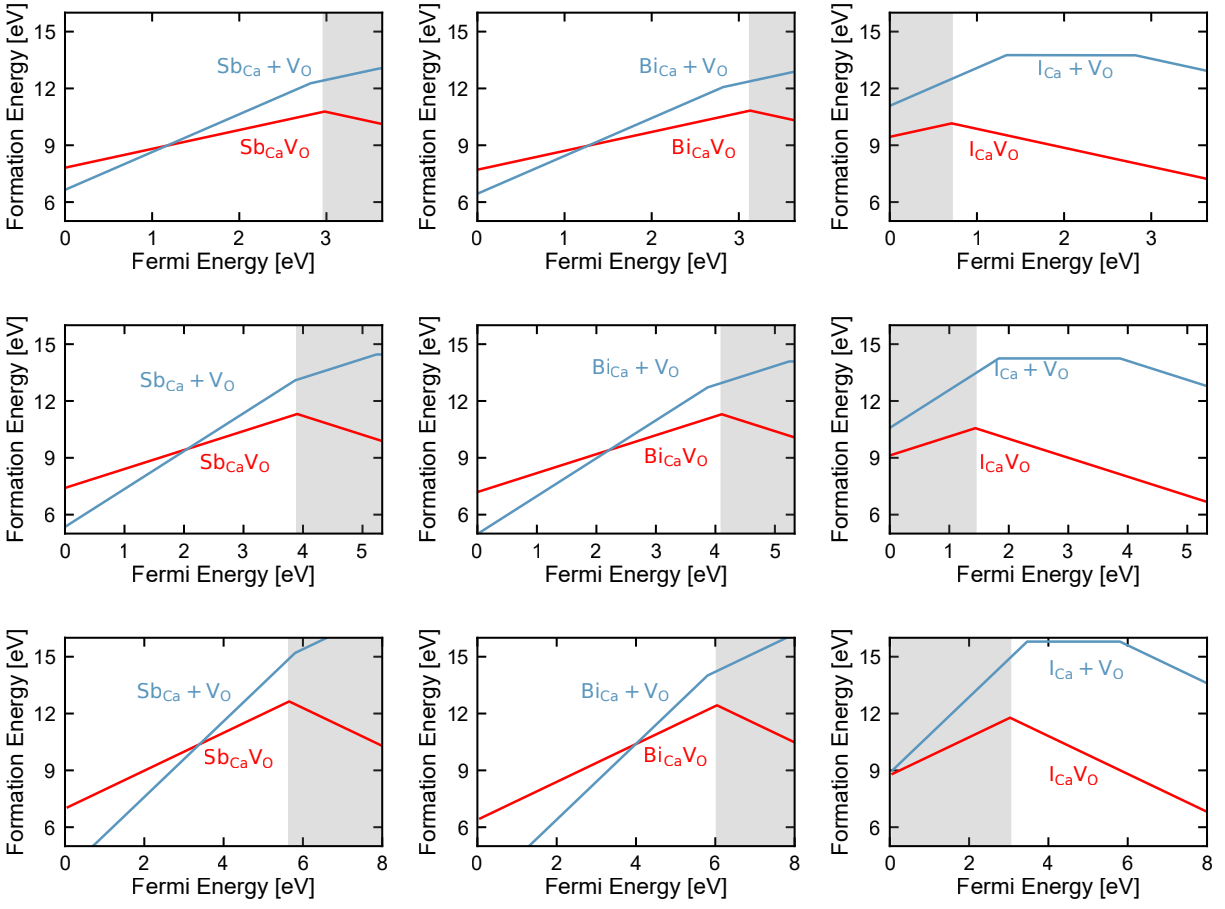
As mentioned in the main text, in the case of P and As dopants, we found two local minima in the total energy of the system, along the path connecting the positions of  $V_{Ca}$  and  $V_O$ . Depending on whether the dopant is initially placed at the Ca or O site, we find different local minima when we optimize the total energy. In the two relaxed structures, the position of the dopants differs by 0.54 Å for P and 0.52 Å for As, see Supplementary Figure 1. Interestingly, for P and As, only the minima closest to the Ca site have the same electronic structure as that of Sb, Bi, and I. These minima correspond to the lowest energy structures, with a difference of 74 meV for the P dopant and 283 meV for the As dopant relative to the metastable minima. However, for the P and As dopants, we could not obtain a satisfactory convergence in the excited states, and due to these difficulties, we omitted these defects from our discussion and focused on the Sb, Bi, and I dopants instead, where only one minimum is found regardless of the starting point of the total energy minimization, and excited states could be properly converged.



Supplementary Figure 1. **The two different minima for the P and As defects.** The left image shows the minimum closest to the Ca site ( $V_{Ca}$ ) and right image the minimum closest to the O site ( $V_O$ ).

## **SUPPLEMENTARY NOTE 2. FORMATION ENERGY OF DEFECTS USING SEMI-LOCAL AND HYBRID FUNCTIONALS**

The formation and binding energies of the Sb, Bi, and I dopants are plotted in Supplementary Figure 2 with the PBE, HSE, and tuned HSE functional. Compared with the PBE results (obtained from ADAQ), the band gap is increased when using HSE06, thus increasing the region of stability for the charge state with spin-1 for all defects considered here. This range of stability is further increased when tuning the short-range Hartree-Fock exchange (more details on the tuned HSE functional are given in the next section). These formation energies are reported with only reference chemical potentials.



Supplementary Figure 2. **Formation energies with semi-local and hybrid functionals.** Formation energy of the  $X_{Ca}V_O$  defects, where  $X = Sb, Bi, I$ . The first row shows the PBE results from ADAQ, the second row shows the HSE06 results, and the third row show the HSE06 results with with 62.5% short-range Hartree-Fock exchange. The shaded regions shows the region of stability for the spin-1 state.

### SUPPLEMENTARY NOTE 3. TUNED SHORT-RANGE HARTREE-FOCK EXCHANGE OF THE HSE06 FUNCTIONAL

Since the HSE06 functional underestimates the band gap of CaO, we tuned the short-range Hartree-Fock exchange to match the experimental band gap following the procedure outlined in Ref. 1. The conventional unit cell was relaxed using a  $3 \times 3 \times 3$  gamma-centered Monkhorst-Pack k-point mesh. A short-range Hartree-Fock exchange of 62.5% gives a lattice parameter of 4.738 Å and a band gap of 7.465 eV. Increasing the k-point mesh to  $5 \times 5 \times 5$  only changes the band gap by 0.01 eV. By subtracting the zero-point renormalization (0.34 eV [2] or 0.36 eV [3]), the band gap is 7.125 or 7.105 eV, a value close to the experimental band gap of 7.09 eV [4]. The Sb, Bi, and I complexes were also investigated with the tuned HSE functional in a  $4 \times 4 \times 4$  supercell with the gamma point only; the results are presented in Supplementary Figure 2. In the following subsections, we discuss different charge corrections and how the choice of chemical potentials affects the stability of single defects as well as growth conditions.



### A. Charge Corrections in DFT Calculations

As mentioned in the main text, to obtain the high-throughput results with the PBE functional, we used the Lany-Zunger (LZ) charge correction for all defects. The correction  $E_{\text{corr}}$  to the total energy is:

$$E_{\text{corr}} = (1 + f) \frac{q^2 \alpha_M}{2\epsilon L}, \quad (1)$$

where  $(1 + f)$  is set to 0.65 [5],  $q$  is the defect charge,  $\alpha_M$  is the Madelung constant that is set to 2.8373 for simple cubic crystals,  $\epsilon = 4\pi\epsilon_0\epsilon_r$  where  $\epsilon_r$  is the dielectric constant (11.95 for CaO), and  $L$  is the length of the supercell (19.315 Å in our PBE simulations). With these values, we obtain  $E_{\text{corr}} = 0.058 \cdot q^2$  eV.

For calculations with the HSE functionals, we used the Freysoldt-Neugebauer-Van de Walle (FNV) correction [6, 7]. Table S1 shows the values of the total energy corrections for the defects considered in our calculations. The FNV corrections are close to the LZ correction of 0.058 eV for single charges and 0.232 eV for double charges. Hence, using the FNV instead of LZ correction amounts to a negligible difference between the computed charge transition levels, due to the large supercell used here and the small values of the defect charge  $q$  ( $q = \pm 1$  and  $q = \pm 2$ ) considered in our study.

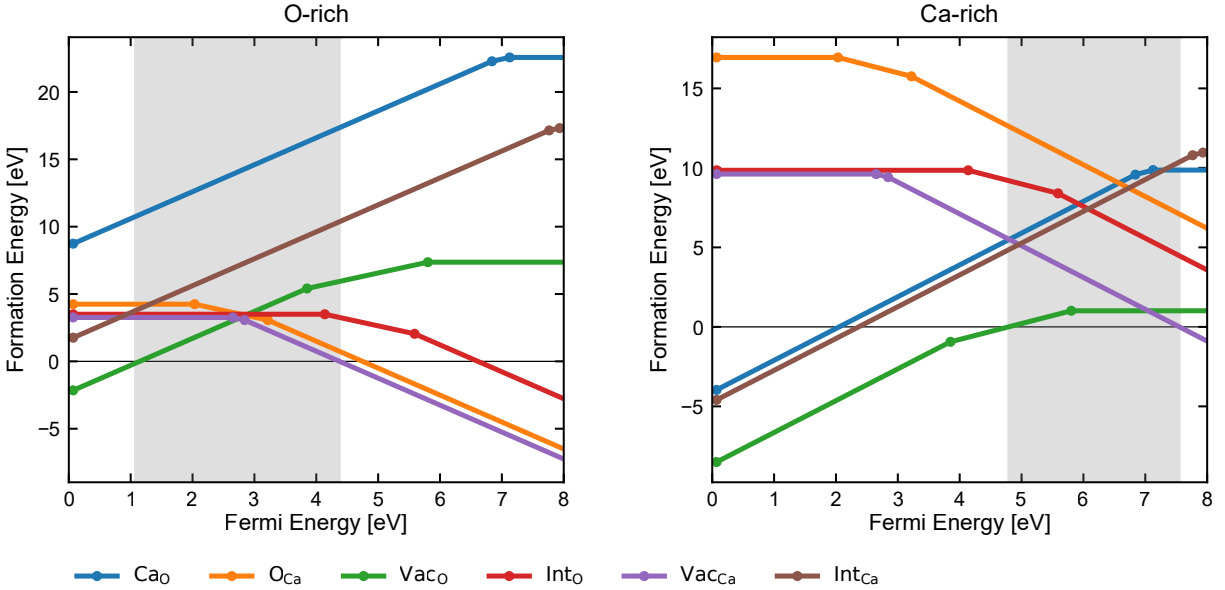
TABLE S1. The FNV correction for the defects in CaO calculated with the HSE functional. C is the long-range potential shift and  $E_{\text{corr}}$  is the correction including screening and alignment.

Defect	charge	C [eV]	$E_{\text{corr}}$ [eV]
$\text{Sb}_{\text{Ca}}\text{V}_{\text{O}}$	+	0.02	0.110193
$\text{Sb}_{\text{Ca}}\text{V}_{\text{O}}$	-	0.03	0.0601929
$\text{Sb}_{\text{Ca}}$	+	0.015	0.105193
$\text{Bi}_{\text{Ca}}\text{V}_{\text{O}}$	+	0.03	0.120193
$\text{Bi}_{\text{Ca}}\text{V}_{\text{O}}$	-	0.03	0.0601929
$\text{Bi}_{\text{Ca}}$	+	0.02	0.110193
$\text{I}_{\text{Ca}}\text{V}_{\text{O}}$	+	0.01	0.100193
$\text{I}_{\text{Ca}}\text{V}_{\text{O}}$	-	0.0	0.0901929
$\text{I}_{\text{Ca}}$	+	0.015	0.105193
$\text{I}_{\text{Ca}}$	-	0.015	0.0751929
$\text{V}_{\text{O}}$	2+	-0.02	0.320772
$\text{V}_{\text{O}}$	+	-0.015	0.0751929
$\text{V}_{\text{Ca}}$	2-	-0.01	0.380772
$\text{V}_{\text{Ca}}$	-	-0.015	0.105193
$\text{O}_{\text{Ca}}$	2-	0.01	0.340772
$\text{O}_{\text{Ca}}$	-	0.01	0.0801929
$\text{Ca}_{\text{O}}$	2+	-0.01	0.340772
$\text{Ca}_{\text{O}}$	+	-0.01	0.0801929
$\text{Int}_{\text{O}}$	2-	-0.04	0.130193
$\text{Int}_{\text{O}}$	-	-0.01	0.100193
$\text{Int}_{\text{Ca}}$	2+	0.0	0.360772
$\text{Int}_{\text{Ca}}$	+	0.01	0.100193

## B. Doping and Growth Conditions of CaO

In oxides, single point defects can have negative formation energy, thus restricting the desired range of Fermi level doping to the region where these defects are stable [8]. In our high-throughput calculations, we considered various single point defects:  $V_{\text{Ca}}$ ,  $V_{\text{O}}$ ,  $\text{Int}_{\text{Ca}}$ ,  $\text{Int}_{\text{O}}$ ,  $\text{Ca}_{\text{O}}$ , and  $\text{O}_{\text{Ca}}$ . Here, V stands for vacancy, and Int for interstitial. These defects, up to double charge states, were investigated with the tuned HSE functional with 62.5% short-range Hartree-Fock exchange.

The chemical potential is defined as  $\mu = \mu_{\text{ref}} + \Delta\mu$ , where  $\mu_{\text{ref}}$  is either the energy of Ca bulk or that of the  $\text{O}_2$  molecule. The  $\Delta\mu$  is bounded by the formation enthalpy of CaO ( $\Delta H_f(\text{CaO})$ ) that is -6.35 eV, which agrees well with other theoretical results (-6.15 eV in Ref. [9]) and the experimental value -6.58 eV [10]. Hence, the two conditions are O-rich ( $\Delta\mu_{\text{O}} = 0$  and  $\Delta\mu_{\text{Ca}} = \Delta H_f(\text{CaO})$ ) and Ca-rich ( $\Delta\mu_{\text{O}} = \Delta H_f(\text{CaO})$  and  $\Delta\mu_{\text{Ca}} = 0$ ) [11]. Supplementary Figure 3 shows the single defects in O- or Ca-rich conditions.

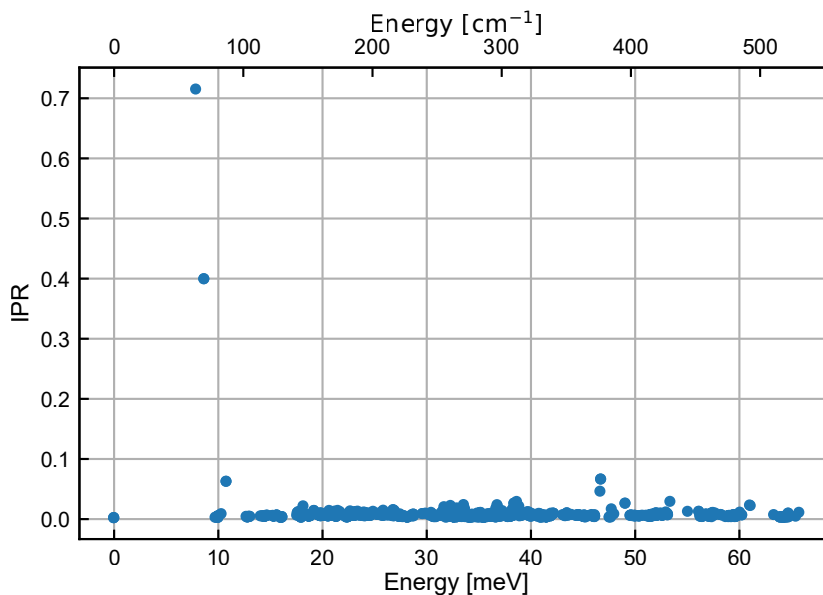


Supplementary Figure 3. **Chemical potential effects on formation energies.** The formation energy of single point defects in CaO calculated with the tuned HSE functional with 62.5% short-range Hartree-Fock exchange for O- or Ca-rich conditions. The shaded regions shows the Fermi energy range where single defects do not spontaneously form.

Supplementary Figure 3 shows the range of Fermi level values where no single defect has negative formation energy. This range is different, depending on the growth conditions: O- or Ca-rich conditions. Our results show that Ca-rich conditions are required to stabilize the Sb and Bi defects in the negative charge state, which has spin-1. Instead, O-rich conditions are required for the I defect to stabilize the positive charge with spin-1. Since the spin-defects proposed here consist of an oxygen and calcium vacancy, their formation energy will decrease with  $\Delta H_f(\text{CaO})$ , regardless of dopants. Supplementary Figure 3 in the main text shows the formation energy and optimal growth conditions for each defect.

## SUPPLEMENTARY NOTE 4. GROUND STATE PHONONS

For the  $\text{Bi}_{\text{Ca}}\text{V}_{\text{O}}^-$  defect, we calculated the phonons of the whole system using phonopy [12, 13], where we enforced a  $C_{4v}$  symmetry for the defect. In the 511 atoms supercell, there were 478 displacements, for which the calculations were carried out with the PBE functional with the same settings as specified in the main text, except that the convergence condition of the total energy was set to  $10^{-8}$  eV and the projection operators were evaluated in reciprocal space. Supplementary Figure 4 shows the inverse participation ratio (ipr) of the phonon eigenmodes as a function of the phonon frequency.



Supplementary Figure 4. **Ground state phonons.** Computed values of the inverse participation ratio (IPR) of the phonon modes as a function of the phonon energy, for a CaO cell with 511 atoms, containing the  $\text{Bi}_{\text{Ca}}\text{V}_{\text{O}}^-$  defect.

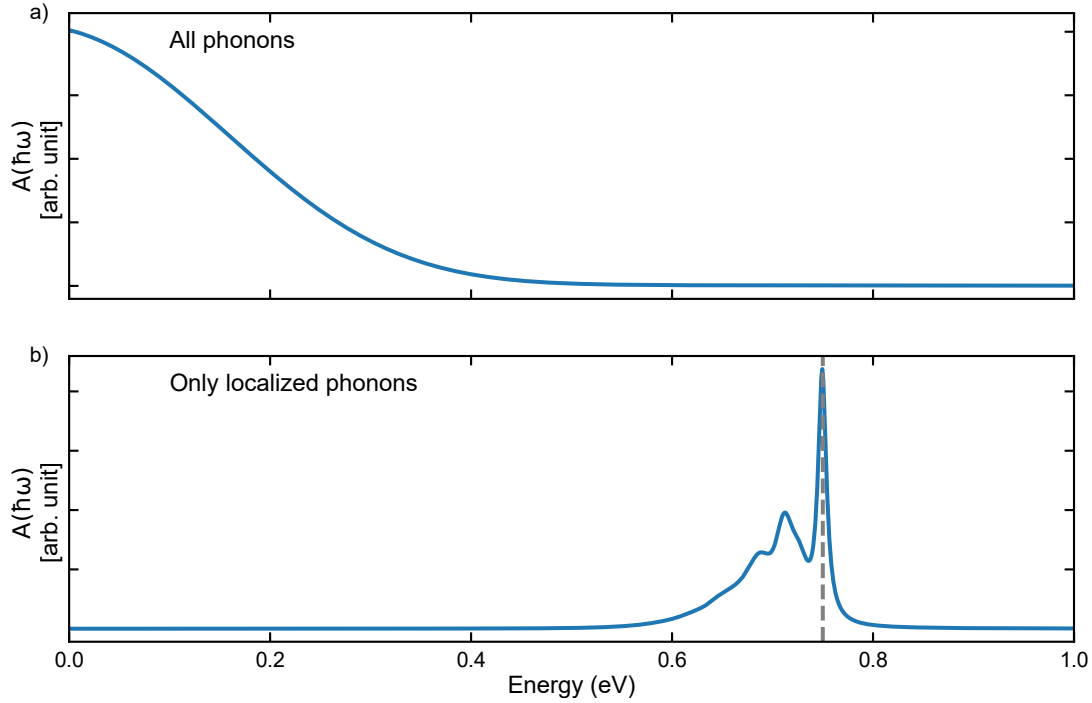
We find that the most localized mode (at 7.8 meV with ipr of 0.71) in the system is mainly localized on the Bi atom and is likely to be a rattling mode. The next highest localized mode (at 8.6 meV and ipr of 0.40) is degenerate, and corresponds to an  $e$  mode.

## SUPPLEMENTARY NOTE 5. PHOTOLUMINESCENCE SPECTRA

We computed photoluminescence (PL) spectra using the method outlined in Ref. 14. The partial Huang-Rhys factors were extracted with pyphotronics [15] using the ground state geometry, computed phonons and excited state geometry. With the PBE functional, the Jahn-Teller splitting between the symmetry-constrained excited state (with half-half occupation) and symmetry-broken excited state (with single occupation) is about 0.1 meV. Hence, we used the symmetry-constrained excited state geometry as often adopted for the NV center in diamond [14].

When considering all phonons, the Huang-Rhys (HR) factor is 19.55 for the  $\text{Bi}_{\text{Ca}}\text{V}_{\text{O}}^-$  defect. However, this large factor may possibly be decreased with nanostructuring, as shown, e.g., in the case of the silicon vacancy in SiC [16], where the Debye-Waller (DW) factor was increased from 6% in bulk to 58% in nanowires. If we assume that reducing the contributions of the bulk phonons is responsible for this improvement, we can do the same for the defect in CaO. if we discard phonons with an ipr below 0.01, we obtain a HR factor of 1.11 (corresponding to a DW factor of 33%). Both spectra with all phonons modes and only localized modes shown in Supplementary Figure 5. Further calculation with better functional and experimental validation are needed to obtain a robust strategy to improve the DW factor.





Supplementary Figure 5. **Simulated photoluminescence spectra.** The emission spectra of the  $\text{Bi}_{\text{Ca}}\text{VO}^-$  defect in CaO with a) all phonon modes and b) only phonons with  $\text{ipr}$  above 0.01. ZPL and phonon broadening parameters are both set to 5 meV.

- 
- [1] Y. Chen, M. E. Turiansky, and C. G. Van de Walle, First-principles study of quantum defect candidates in beryllium oxide, *Phys. Rev. B* **106**, 174113 (2022).
  - [2] A. Miglio, V. Brousseau-Couture, E. Godbout, G. Antonius, Y.-H. Chan, S. G. Louie, M. Côté, M. Giantomassi, and X. Gonze, Predominance of non-adiabatic effects in zero-point renormalization of the electronic band gap, *npj Computational Materials* **6**, 167 (2020).
  - [3] M. Engel, H. Miranda, L. Chaput, A. Togo, C. Verdi, M. Marsman, and G. Kresse, Zero-point renormalization of the band gap of semiconductors and insulators using the projector augmented wave method, *Phys. Rev. B* **106**, 094316 (2022).
  - [4] R. Whited, C. J. Flaten, and W. Walker, Exciton thermoreflectance of mgo and cao, *Solid State Communications* **13**, 1903 (1973).
  - [5] S. Lany and A. Zunger, Assessment of correction methods for the band-gap problem and for finite-size effects in supercell defect calculations: Case studies for zno and gaas, *Phys. Rev. B*

- 78**, 235104 (2008).
- [6] C. Freysoldt, J. Neugebauer, and C. G. Van de Walle, Fully ab initio finite-size corrections for charged-defect supercell calculations, *Phys. Rev. Lett.* **102**, 016402 (2009).
  - [7] C. Freysoldt, J. Neugebauer, and C. G. Van de Walle, Electrostatic interactions between charged defects in supercells, *physica status solidi (b)* **248**, 1067 (2011), <https://onlinelibrary.wiley.com/doi/pdf/10.1002/pssb.201046289>.
  - [8] J. Robertson and S. J. Clark, Limits to doping in oxides, *Phys. Rev. B* **83**, 075205 (2011).
  - [9] J. Osorio-Guillén, S. Lany, S. V. Barabash, and A. Zunger, Magnetism without magnetic ions: Percolation, exchange, and formation energies of magnetism-promoting intrinsic defects in cao, *Phys. Rev. Lett.* **96**, 107203 (2006).
  - [10] W. M. Haynes, D. R. Lide, and T. J. Bruno, *CRC handbook of chemistry and physics*, 95th ed. (CRC press, 2016).
  - [11] C. Freysoldt, B. Grabowski, T. Hickel, J. Neugebauer, G. Kresse, A. Janotti, and C. G. Van de Walle, First-principles calculations for point defects in solids, *Rev. Mod. Phys.* **86**, 253 (2014).
  - [12] A. Togo, L. Chaput, T. Tadano, and I. Tanaka, Implementation strategies in phonopy and phono3py, *J. Phys. Condens. Matter* **35**, 353001 (2023).
  - [13] A. Togo, First-principles phonon calculations with phonopy and phono3py, *J. Phys. Soc. Jpn.* **92**, 012001 (2023).
  - [14] A. Alkauskas, B. B. Buckley, D. D. Awschalom, and C. G. V. de Walle, First-principles theory of the luminescence lineshape for the triplet transition in diamond nv centres, *New Journal of Physics* **16**, 073026 (2014).
  - [15] S. A. Tawfik and S. P. Russo, Pyphotronics: A python package for the evaluation of luminescence properties of defects, *Computer Physics Communications* **273**, 108222 (2022).
  - [16] J. H. Lee, W. B. Jeon, J. S. Moon, J. Lee, S.-W. Han, Z. Bodrog, A. Gali, S.-Y. Lee, and J.-H. Kim, Strong zero-phonon transition from point defect-stacking fault complexes in silicon carbide nanowires, *Nano Letters* **21**, 9187 (2021).